JOURNAL OF MULTIFUNCTIONAL MATERIALS & PHOTOSCIENCE
9(1), June 2018, pp. 115-138

# An Alternative Graphene Composites and Perovskite Material as a Counter Electrode Dye-sensitized Solar Cells for Renewable Energy

**Yonrapach Areerob and Won-Chun Oh[a*]**

[a] *Department of Advanced Materials Science & Engineering, Hanseo University, Seosan-si, Chungcheongnam-do, 31962, South Korea*

***Abstract:*** The dye-sensitized solar cell (DSSC) plays a leading role in third generation photovoltaic devices. Platinum-loaded conducting glass has been widely exploited as the standard counter electrode (CE) for DSSCs. However, the high cost and the rarity of platinum limits its practical application in DSSCs. This has promoted large interest in exploring Pt-free CEs for DSSCs. Very recently, graphene, which is an atomic planar sheet of hexagonally arrayed $sp^2$ carbon atoms, has been demonstrated to be a promising CE material for DSSCs due to its excellent conductivity and high electrocatalytic activity. This article provides a mini review of graphene-based CEs for DSSCs. Firstly, the fabrication and performance of graphene film CE in DSSCs are discussed. Secondly, DSSC counter electrodes made from graphene-based composite materials are evaluated. Finally, a brief outlook is provided on the future development of graphene-based materials as prospective counter electrodes for DSSCs.

## 1. Introduction

To deal with global energy challenge and environment crisis, one of most promising technologies in the field of electrochemical energy storage and conversion is the conversion of sustainable and clean solar energy directly into electricity using photovoltaic devices. The various photovoltaic devices mainly include silicon based solar cells **[1, 2]**, organic solar cells **[3, 4]**, and dye- sensitized solar cells **[5, 6].**

DSSCs are expected to be one of the next generation of solar cells because of their low fabrication cost, simple structure and use of raw materials **[7]**, as well as the fact that they operate on the same principle as photosynthesis in plants. In DSSCs, an electron is moved from the excited dye acting as a sensitizer to the conduction band of a metal oxide. Then, the negative charge diffuses outside of the transparent conductive oxide (TCO) glasses because of the excess concentration of electrons in the conduction band of the metal oxide **[8]**. A maximum efficiency of 11% was achieved for DSSCs by Gratzel *et al.* **[9]**.

A classical DSSC consists of a dye-sensitized nanocrystalline titanium dioxide ($TiO_2$) film, an electrolyte containing iodide/triiodide ($I^-/I_3^-$) redox couples, and a Pt counter

* Corresponding author*: wc_oh@hanseo.ac.kr*

electrode (CE). As one of major components, the counter electrode collects electrons from external circuit and reduces the triiodide $I_3^-$ to iodide $I^-$, which acts as a mediator in regenerating the sensitizer after the electrons injection. A fast reduction reaction at the counter electrode to suppress the charge recombination process at the photoanode can be greatly responsible for a high-performance DSSC, since the photoanode and counter electrode are both exposed to the electrolyte **[10]**. Therefore, in consideration of its important role for efficient DSSC, the ideal counter electrode material is expected to have good electrical conductivity, excellent catalytic activity, and superior chemical stability.

Pt is commonly used as counter electrode material due to its outstanding electrical conductivity and catalytic properties, but the high cost and corrosive properties in the electrolyte of Pt hindered its practical application in the long-term DSSC device **[11]**. Currently, the hot issues are to seek for the economical and highly catalytic materials to replace Pt for the sustainable development. Several varieties of low-cost candidates, such as car- bonaceous materials **[12]**, conductive polymers **[13]**, alloys **[14]**, metal oxide **[15]**, transition metal based materials including metal carbides **[16]**, metal nitrides **[17]**, and metal sulfides **[18]** have been widely investigated as novel counter electrode alternatives and demonstrated outstanding catalytic performance for the triiodide reduction. In particular, carbonaceous materials such as graphite, carbon black, activated carbon, mesoporous carbon, carbon nanotubes and fullerenes have attract more attention compared to other counter electrode materials, due to their relatively low cost, good stability, and high catalytic ability **[19]**. Nevertheless, in most cases, their electrical conductivities and reduction catalytic activities still cannot match up to those of Pt. Obviously, the major concerns are an optimization of physical and chemical properties of carbon materials to further enhance their catalytic activity for high-performance DSSC.

## 2. Structure and Materials

The schematic structure of the DSSC constructed by the Gratzel group is shown in Figure 1. The composition of the DSSC is described in this section.

### *2.1. Transparent conducting oxide-coated glass substrate*

Transparent conducting oxide (TCO) coated glass is used as the substrate for the $TiO_2$ photoelectrode. For high solar cell performance, the substrate must have low sheet resistance and high transparency. In addition, sheet resistance should be nearly independent of the temperature up to 500 °C because sintering of the $TiO_2$ electrode is carried out at 450 to 500 °C. Indium–tin oxide (ITO) is one of the most famous TCO materials. In spite of having low resistance at room temperature, ITO resistance increases significantly at high temperature in air. Usually, fluorine-doped $SnO_2$ is used as the TCO substrate for DSSCs (e.g. Nippon Sheet Glass Co., R = 8–10 W /square).

### *2.2. $TiO_2$ photoelectrode*

Photoelectrodes made of such materials as Si, GaAs, InP, and CdS decompose under irradiation in solution owing to photocorrosion. In contrast, oxide semiconductor materials,

especially $TiO_2$, have good chemical stability under visible irradiation in solution; additionally, they are nontoxic and inexpensive. The $TiO_2$ thin-film photoelectrode is prepared by a very simple process. $TiO^2$ colloidal solution (or paste) is coated on a TCO substrate and then sintered at 450 to 500 °C, producing a $TiO_2$ film about 10 ìm in thickness. Because this film is composed of $TiO_2$ nanoparticles (10–30 nm), giving it a nanoporous structure, the actual surface area of $TiO_2$ compared to its apparent surface area, roughness factor (rf), is >1000; that is, a 1-$cm^2$ $TiO_2$ film (10 μm thickness) has an actual surface area of 1000 $cm^2$. The dye is considered to be adsorbed on the $TiO_2$ surface in a mono- layer **[20]**. Thus, if the nanoporous $TiO_2$ film has a high rf, the amount of dye adsorbed is drastically increased (on the order of 10–7 mol $cm^{-2}$), resulting in an increase of LHE that is near 100% at the peak absorption wavelength of the dye. In comparison, the amount of adsorbed dyes on the surface of single-crystal and polycrystal materials is quite small, with only 1% LHE even at the peak wavelength.

Normally, the $TiO_2$ film contains large $TiO_2$ particles (250–300 nm), which can scatter incident photons effectively, to improve the LHE as shown later. The porosity of the film is also important because the electrolyte, which contains the redox ions, must be able to penetrate the film effectively to suppress the rate-determining step via diffusion of redox ions into the film. Appropriate porosity, 50 to 70%, is controlled in the sintering process by the addition of a polymer such as polyethylene glycol (PEG) and ethyl cellulose (EC) into the $TiO_2$ colloidal solution or paste. Figure 2 shows a scanning electron microscope (SEM) photograph of a typical nanocrystalline $TiO_2$ film.

### *2.3. Ru complex photosensitizer*

The Ru complex photosensitizer, which contributes the primary steps of photon absorption and the consequent electron injection, is adsorbed onto the $TiO_2$ surface. The chemical structure of typical Ru complex photosensitizers developed by Gra tzel's group are shown in Figure 3 (TBA is tetrabutylammonium cation, $(C_4H_9)4N^+$), and Figure 4 shows absorption properties of the complexes in solution. The y-axis is represented by absorbance (A) and 1 – T (= 1 – 10–A), where T is the transmittance. The cis-bis(4,4′ - dicarboxy-2,2′ - bipyridine)dithiocyanato ruthenium(II) ($RuL_2(NCS)_2$ complex), which is referred to as N3 dye (or red dye), can absorb over a wide range of the visible regions from 400 to 800 nm. The trithiocyanato 4,4′4″ -tricarboxy-2,2′:6′,2″-terpyridine ruthenium(II) (black dye) ($RuL'(NCS)_3$ complex), absorbs in the near-IR region up to 900 nm. Absorption by these dyes in the visible and near-IR regions is attributed to the metal-to-ligand charge-transfer (MLCT) transition **[21]**. The highest occupied molecular orbital (HOMO) and the lowest unoccupied molecular orbital (LUMO) are mainly derived from the d-orbitals of the Ru metal and the π″ orbital of the ligand, respectively. The NCS ligand shifts the HOMO level negatively, leading to a red shift in the absorption property of the complex, and also contributes electron acceptance from reduced redox ions ($I^-$). These Ru complexes have carboxyl groups to anchor to the $TiO_2$ surface. Anchoring causes a large electronic interaction between the ligand and the conduction band of $TiO_2$, resulting in effective electron injection from the Ru complex into the $TiO_2$. The Ru complex is adsorbed on the

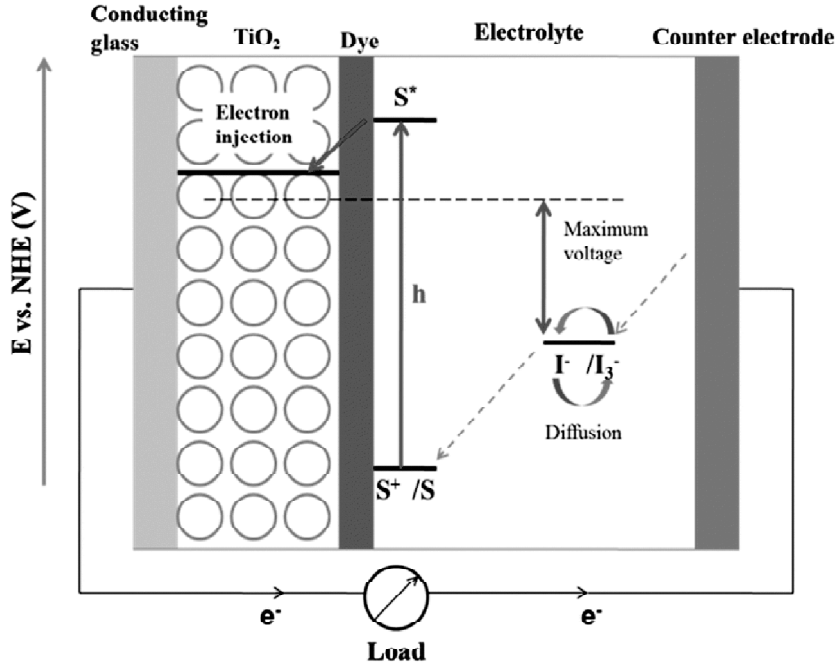


**Figure 1:** A schematic of a DSSC in principle

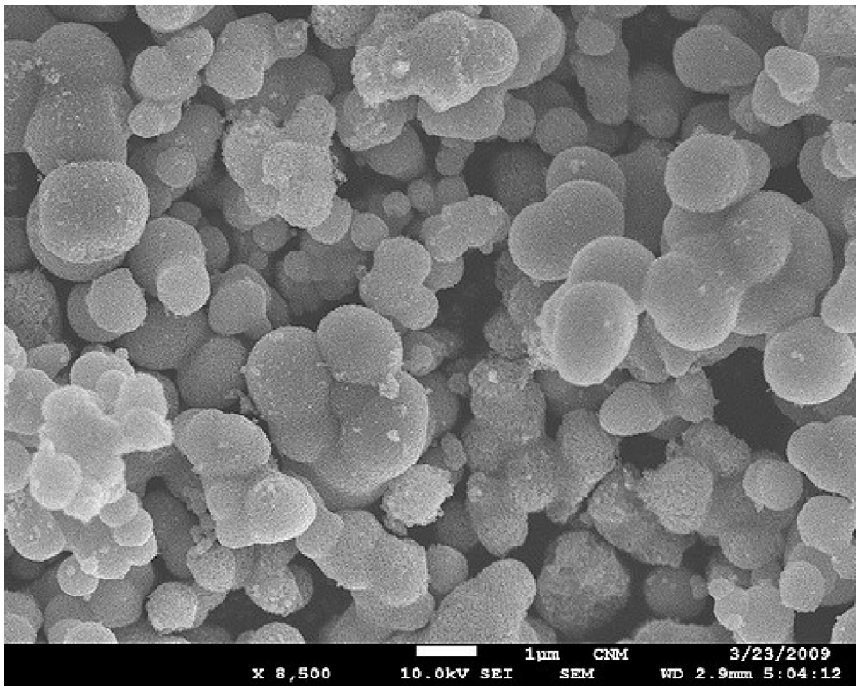


**Figure 2:** Scanning electron microscope photograph of a typical nanocrystalline $TiO_2$ film: the scale bar corresponds to 0.43 μm

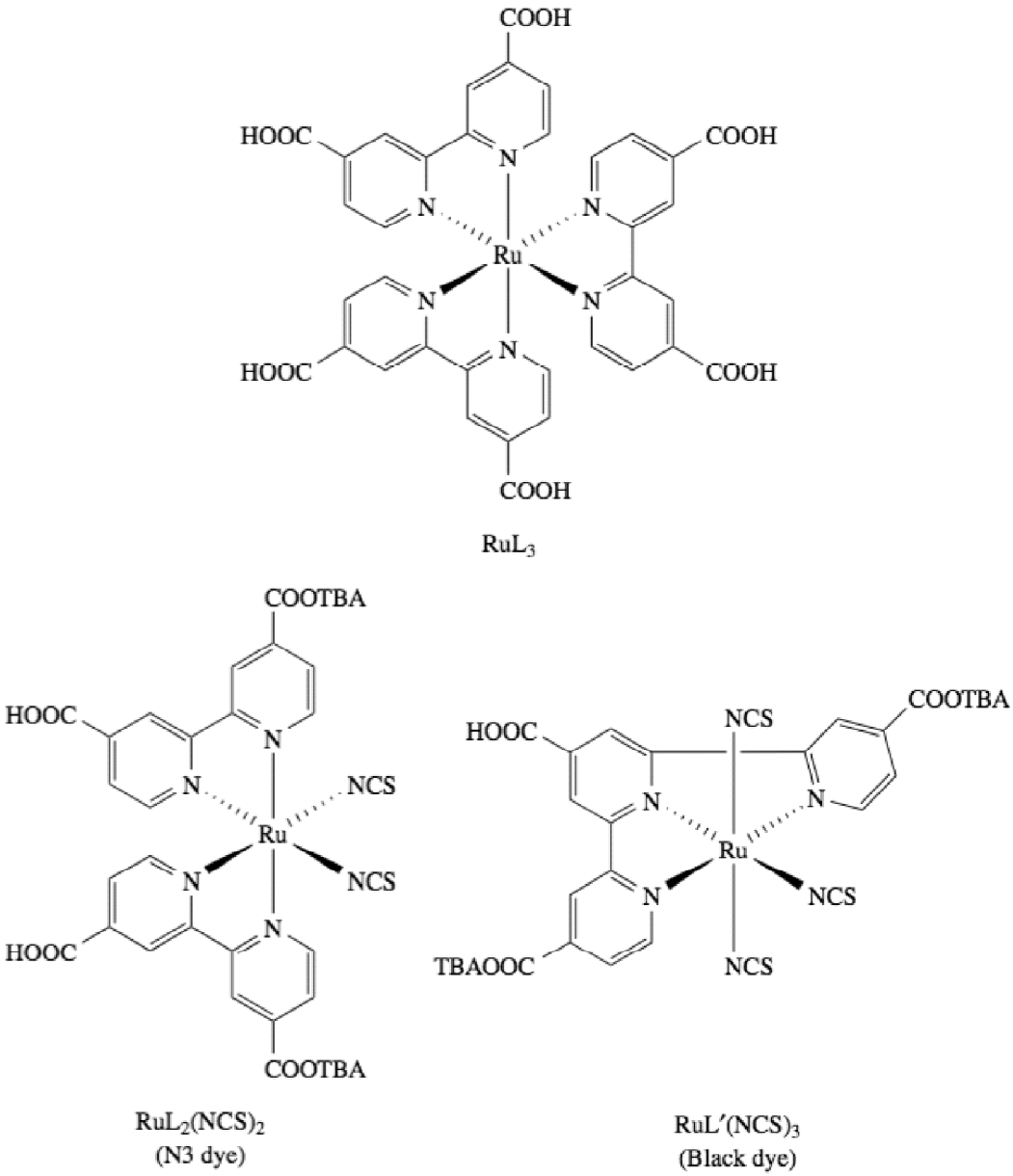


**Figure 3:** Molecular structures of typical Ru complex photosensitizers

$TiO_2$ surface via either carboxylate bidentate coordination or ester bonding (–C(=O)O–) as measured by FT–IR absorption analysis **[22]**. Figure 5 shows the anchoring structure of the N3 dye adsorbed on the (101) surface of $TiO_2$. The coverage of the $TiO_2$ surface with the N3 dye reaches near 100% as derived from the surface area of $TiO_2$ and the amount of the dye.

### *2.4. Redox electrolyte*

The electrolyte used in the DSSC contains $I^-/I_3^-$ redox ions, which mediate electrons between the $TiO_2$ photoelectrode and the counter electrode. Mixtures of iodides such as LiI, NaI, KI, tetraalkylammonium iodide ($R_4NI$), and imidazolium-derivative iodides with concentrations of 0.1 to 0.5 M (M: molar concentration) and 0.05 to 0.1 M $I_2$ dissolved in nonprotonic solvents (e.g. acetonitrile, propionitrile, methoxyacetonitrile, propylene carbonate, and their mixture) are employed. Cell performance of DSSCs depends on counter cations of iodides such as Li+ , Na+ , K+ , and R4 $N^+$ owing to different ion conductivity in the electrolyte or adsorption on the $TiO_2$ surface, leading to a shift of the conduction-band level of the $TiO_2$ electrode **[23]**. Viscosity of solvents directly affects ion conductivity in the electrolyte, and consequently the cell performance. To improve cell performance, low-viscosity solvents are desired. The diffusion coefficient of $I_3^-$ in methoxyacetonitrile is estimated as $5.4 - 6.2 \times 10^{-6}$ $cm^2$ $s^{-1}$. Basic compounds such as tert-butylpyridine are added to the electrolyte solution to improve cell performance, as shown later. $Br^-/Br_2$ and hydroquinone have also been used as redox electrolyte for DSSC, but the iodine redox electrolyte gives the best performance.

### *2.5. Counter electrode*

Tri-iodide ions, $I_3^-$, formed by the reduction of dye cations with $I^-$ ion, are re-reduced to $I^-$ ions at the counter electrode. To reduce the tri-iodide ions, the counter electrode must have high electrocatalytic activity. Pt coated on TCO substrate (5–10 $\mu gcm^{-2}$ or approximately 200-nm thickness) or carbon are usually used as the counter electrode.

### *2.6. Sealing materials*

A sealing material is needed to prevent the leakage of the electrolyte and the evaporation of the solvent. Chemical and photochemical stability of the sealing material against the electrolyte component, iodine, and the solvent is required. Surlyn (Du Pont), a copolymer of ethylene and acrylic acid, meets these requirements.

## 3. DSSC counter electrodes

A typical dye-sensitized solar cell consists of a dye-sensitized nanocrystalline $TiO_2$ film as the photoanode, a counter electrode (CE) and an electrolyte with a redox couple in the liquid or solid state **[24]**. The CEs task is to reduce redox species in liquid solar cells, which are used as mediators in the regeneration of the sensitizer after electron injection, or to collect holes from the hole conducting material in solid-state DSSCs. For an optimized cell, one must choose a CE material with the lowest possible sheet resistance, excellent catalytic activity for the reduction of the redox electrolyte, high chemical stability and a low cost.

The tri-iodides are produced near the dye-sensitized $TiO_2$ electrode and reduced at the counter electrode. Platinum-loaded conducting glass has been widely employed as the standard CE for DSSCs due to its high catalytic activity and excellent conductivity as

well as its high corrosion stability against iodine in the electrolyte **[25]**. However, the combination between the limited resource of platinum and the large application of platinum-based catalysts in the vehicle industry makes platinum extremely expensive and in diminishing supply. Therefore, it is important to explore Pt-free materials to replace the Pt counter electrode for DSSCs . For this reason, recent attention has been focused on various materials as potential alternatives to Pt, including carbon **[26]**, transition metal sulfides **[27]**, nitrides **[28]** and carbides **[29]**.

Kay and Gratzel first explored a graphite/carbon black mixture as a counter electrode **[30]** due to its low cost and abundance. This pioneering work stimulated intensive researche to evaluate various types of carbon for DSSC counter electrodes. It was reported that, under AM 1.5 simulated sunlight, energy conversion efficiencies were 6.67, 3.9, 4.5 and 7.7% for DSSCs with counter electrodes of graphite, 43 activated carbon, 44 single-walled carbon nanotubes (SWCNTs) and multi-walled carbon nanotubes (MWCNTs) **[31]**, respectively. Furthermore, DSSC with large effective surface-area polyaromatic hydrocarbon (LPAH) counter electrodes achieved an energy conversion efficiency of 7.89%. Currently, the main drawback of carbon-based counter electrodes is the requirement of a large amount of carbon to reach comparable efficiencies to Pt-based CEs. This makes the device bulkier and more opaque. As a rising star in the carbon family, graphene, with its unique properties, is being explored as a DSSC counter electrode to solve these issues.

## 4. Graphene-based counter electrodes for DSSCs

Graphene was expected to be a promising material for DSSC counter electrodes due to its excellent conductivity that can decrease charge transfer resistance ($R_{ct}$). Kaniyoor and Ramaprabhu showed that the $R_{ct}$ of thermally exfoliated graphene (TEG) films is 11.7 W $cm^2$, which is very close to that of Pt electrodes (6.5 W $cm^2$). The DSSCs fabricated with TEG as a counter electrode exhibited a power conversion efficiency of about 2.8%, comparable to that (about 3.4%) of Pt-based DSSCs. Furthermore, Zhang *et al.* **[32]** made similar observations, namely, the $R_{ct}$ value of graphene nanosheet (GN) films is close to that of Pt, resulting in comparable efficiencies between the DSSCs using GNs and Pt as counter electrodes. So far, several groups have explored graphene-based counter electrodes. **[33]** From Table 1, one can see that the reported efficiencies of DSSCs fabricated with graphene counter electrodes vary from 0.7 to 6.8%. The difference in the efficiency with graphene counter electrodes is mainly due to the utilization of different techniques for the graphene film preparation and the DSSC fabrication. Graphene films for DSSC counter electrodes have been formed by various techniques, including thermal exfoliation from graphite oxide, the oxidative exfoliation of graphite followed by hydrazine reduction, the chemical reduction of graphene oxide colloids under microwave irradiation and electrophoretic deposition (EPD) followed by an annealing treatment. So far, the best DSSC efficiency (6.8%) has been obtained with a graphene counter electrode fabricated via the following approach: graphene nanosheets (GN), which were synthesized by a hydrazine reduction of exfoliated graphene oxide, were ground in a terpineol solution and then deposited on a FTO glass, followed by annealing in air. It was shown that the

**Table 1**
**PV characteristics of DSSCs fabricated with graphene counter electrodes**

| *Sample* | *Jsc(mA cm$^{-2}$)* | *Voc(V)* | *FF* | *η(%)* | *Ref.* |
|---|---|---|---|---|---|
| Graphene | 7.70 | 0.68 | 0.54 | 2.82 | 49 |
| Graphene | 16.98 | 0.74 | 0.53 | 6.81 | 50 |
| Graphene | 6.12 | 0.64 | 0.56 | 2.19 | 51 |
| Graphene | 5.60 | 0.70 | 0.60 | 2.30 | 52 |
| Graphene | 14.30 | 0.54 | 0.65 | 5.69 | 53 |
| Graphene | 8.11 | 0.72 | 0.46 | 2.64 | 54 |
| Graphene | 6.42 | 0.70 | 0.16 | 0.74 | 55 |

annealing temperature used for the GN-based counter electrode exhibited a remarkable effect on the performance of DSSCs, namely, the PV performance increased and then dropped with an increasing annealing temperature (Fig. 6). The optimized annealing temperature was 400° C, at which the best performance was achieved. The best cell showed a short-circuit current ($J_{SC}$) of 17 mA cm$^{-2}$, an open-circuit voltage ($V_{OC}$) of 0.747 V and a fill factor (*FF*) of 53.62% under the illumination of 100 mW cm$^{-2}$, leading to a high energy conversion efficiency of 6.8%. It was found that there was a trade-off between enhancing the adhesion and increasing the electrical conductivity of the GN film on the FTO glass by the annealing treatment in air. When the annealing temperature was higher than 400 °C, the GN film was easier to peel off from the substrate due to the presence of fewer organic

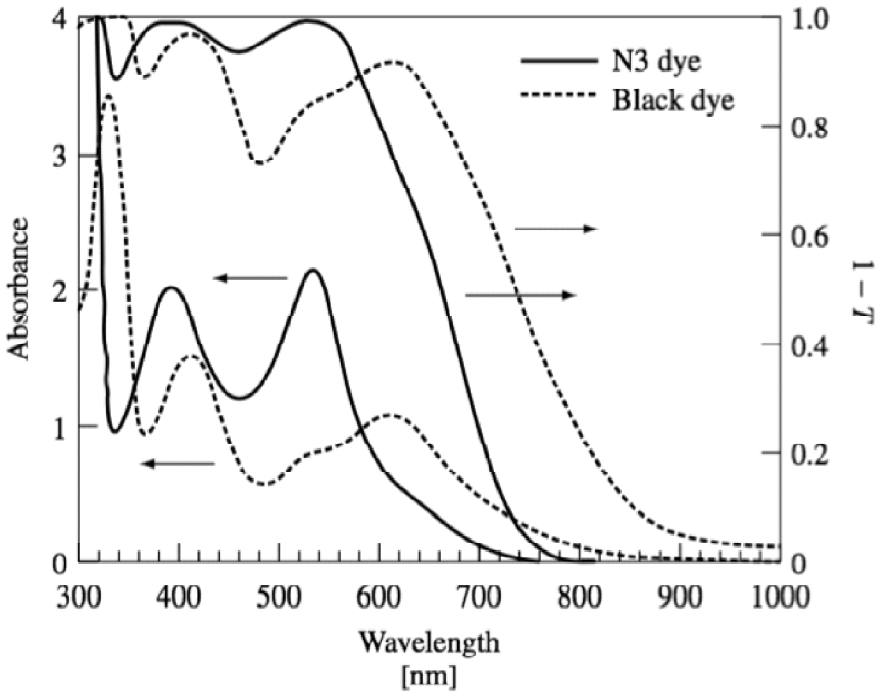


**Figure 4:** Absorption spectra of N3 dye and black dye represented by absorbance and light-harvesting efficiency, 1–T (T: transmittance): ( -) N3 dye, ( — —) black dye

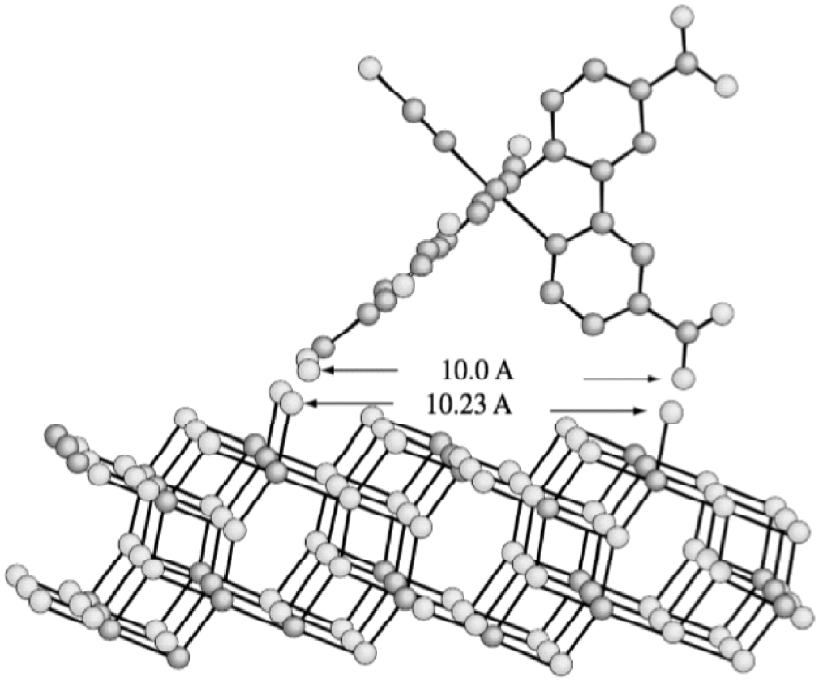


**Figure 5:** Anchoring structure of N3 dye adsorbed on the (101) surface of $TiO_2$: the top is N3 dye and the bottom is $TiO_2$. Reprinted with permission from (2002) American Chemical Society

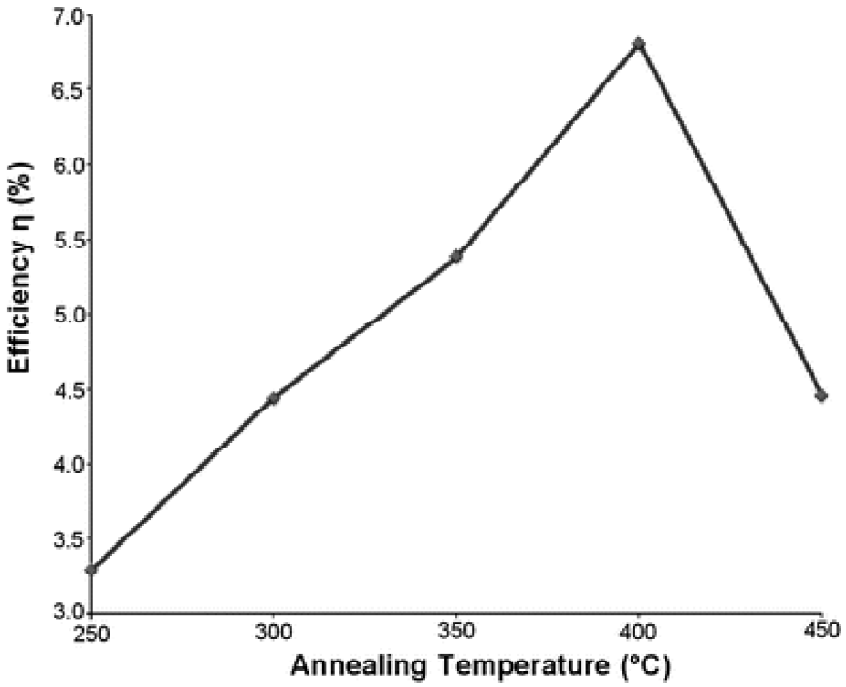


**Figure 6:** Power conversion efficiency (h) of DSSCs vs. annealing temperature of the counter electrodes

binders (terpineol and ethyl cellulose), which were burned out at high temperatures, causing a higher $R_{ct}$ in the counter electrode.

The performance of a DSSC with a graphene counter electrode is dependent on the structure of graphene. Perfect graphene has an extremely high conductivity, but it may possess a limited number of active sites for $I^-/I_3^-$ electrocatalysis. Kavan et al. demonstrated that the electrocatalytic activity of graphene nanosheets is usually associated with its defects and oxygen-containing functional groups. **[34]** It is well known that lattice surface defects exist in graphene sheets prepared from graphite via an oxidation– reduction approach. Lattice defects are considered as electrocatalytic active sites. On the other hand, Roy-Mayhew et al. found that increasing the number of oxygen-containing functional groups in a graphene sheet enhanced its electrocatalytic activity for $I_3^-$ reduction. **[35]** Furthermore, Xu et al. reported that reduced graphene oxide (RGO) functionalized with –NHCO– groups exhibited a higher catalytic ability than the original RGO. This indicates that –NHCO– groups can increase catalytic activity. However, it is still unclear what specific oxygen-containing functional groups in the RGO sheets are mainly responsible for the $I^-/I_3^-$ electrocatalysis. In addition, it was found that the DSSC with the counter electrode, which was made from partially reduced graphene oxide, exhibited a low conversion efficiency equal to 40% that of a Pt-based cell.59 This happened because the partially reduced graphene oxide had too many oxygen-containing groups, which decreased the electrical conductivity of graphene. **[36]** Therefore, one must make a balance between the electrical conductivity and the electrocatalytic activity of graphene to optimize the DSSC by functionalization.

Graphene possesses an excellent mechanical flexibility. Tung *et al.* **[37]** showed that, after bending to 60 more than 10 times, the electrical resistance of a graphene film remained almost unchanged, whereas the resistance of the brittle indium tin oxide (ITO) film was increased by a factor of 3. Furthermore, Lee *et al.* demonstrated that a DSSC with a graphene-based counter electrode exhibited almost the same cell performances before and after bending of the electrode. In contrast, for a DSSC with an ITO based counter electrode, the performance was greatly degraded after the bending treatment. This indicates that graphene can be exploited to fabricate flexible counter electrodes for DSSCs.

## 5. Graphene-based composites for counter electrodes

### *5.1. Graphene/polymer composites*

Since the composite materials of graphene with conductive polymers were first reported by Stankovich et al. in 2006, **[38]** graphene-based composite materials have attracted much attention. Recently, graphene/conductive polymer composite films have been employed as counter electrodes in DSSCs. In the composite films, the polymer can act as a conductive support, with graphene being responsible for catalysis. As shown in Fig. 7a, the graphene sheets were dispersed uniformly in the (3,4-ethylenedioxythiophene) poly (styrenesulfonate) (PEDOT-PSS) matrix due to strong static interactions between 1-pyrenebutyrate ($PB^-$) functionalized graphene sheets and the PEDOT chains. In this composite

system, graphene sheets can provide high catalytic activity toward the reduction of iodine, while PEDOT-PSS can form a highly conductive matrix around the graphene sheets. The DSSC with such a graphene/PEDOT- PSS counter electrode exhibited an efficiency of 4.5%, which is higher than that (2.3%) of the DSSC with a PEDOT-PSS counter electrode in the absence of graphene (Table 2).

**Table 2**
**PV characteristics of DSSCs fabricated with graphene/polymer composite counter electrodes**

| *Counter electrode* | *Jsc(mA cm$^{-2}$)* | *Voc(V)* | *FF* | *h(%)* |
|---|---|---|---|---|
| Graphene/PEDOT | 12.96 | 0.72 | 0.48 | 4.50 |
| Pt | 13.05 | 0.72 | 0.28 | 6.30 |
| PEDOT-PSS | 10.99 | 0.72 | 0.68 | 2.30 |
| Graphene/PANI | 13.28 | 0.68 | 0.67 | 6.09 |
| Pt | 14.20 | 0.69 | 0.70 | 6.88 |
| PANI | 12.86 | 0.68 | 0.54 | 4.78 |
| Pt/ITO | 12.60 | 0.77 | 0.63 | 6.26 |

On the other hand, graphene sheets can also be used as a support for conductive polymers. To disperse a conductive polymer on graphene sheets, Wang *et al.* **[39]** synthesized polyani- line (PANI) on graphene sheets as a nanocomposite material by an in situ polymerization technique. As a result, the graphene sheets were homogeneously coated with polyaniline nano- particles (Fig. 7b). The DSSC, which was fabricated with the PANI/graphene counter electrode, achieved a high conversion efficiency of 6.09%, which is close to that (6.88%) of the corresponding cell with a Pt counter electrode. Lee et al. dispersed PEDOT on a graphene layer as a counter electrode. **[39]** The DSSC with such a graphene/PEDOT composite counter electrode showed a high efficiency of 6.26%. This occurred because the incorporation of graphene into PEDOT resulted in, not only the superior electrochemical activity, but also much faster transport through the composite film.

### *5.2. Graphene/metal composites*

A strategy to reduce Pt loading in DSSCs is to exploit Pt/graphene composite materials as counter electrodes. Gong et al. synthesized a Pt/graphene composite (Fig. 8(a)) via the self-assembly of polyelectrolyte, graphene and $H_2PtCl_6$, followed by an annealing treatment. **[40]** The DSSC with the Pt/graphene composite as a counter electrode achieved a power conversion efficiency of 7.66%, comparable to that (8.16%) of the DSSC with a sputtered-Pt counter electrode. Importantly, the Pt/graphene counter electrode contained much less Pt than the sputtered-Pt electrode, leading to a dramatic decrease in the DSSC fabrication cost. Furthermore, the effect of Pt loading on the PV performance of the DSSCs was evaluated by Bajai *et al.* **[41]** They deposited Pt nanoparticles on graphene layers using a pulsed laser ablation method (Fig. 8b) and revealed that the amount of Pt loading had a remarkable influence on the efficiency of the resulting DSSCs. An optimized Pt loading (27.43%) was obtained. The DSSC with the optimized Pt/graphene counter

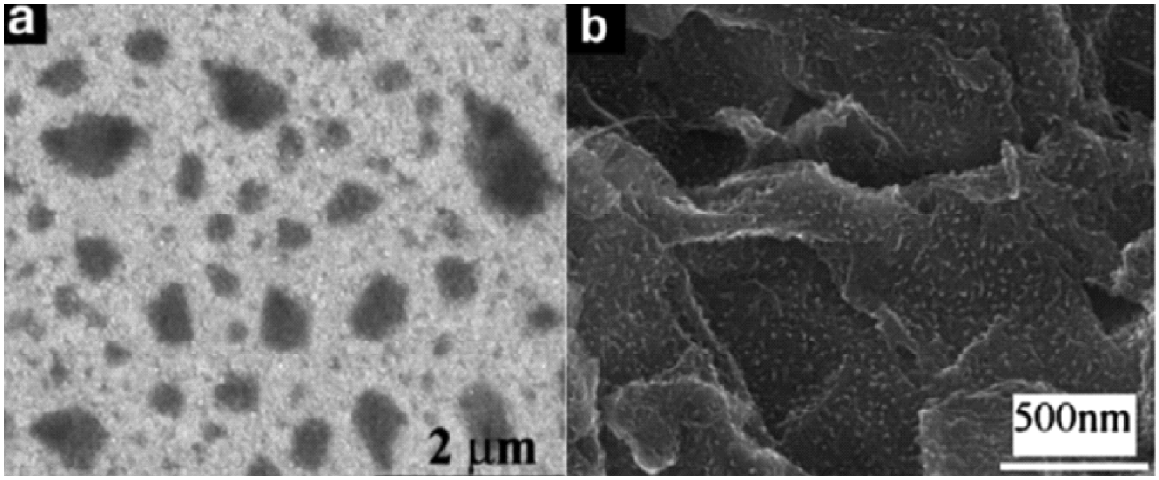


**Figure 7:** SEM images of (a) the graphene/PEDOT-PSS composite and (b) the graphene/PANI composite

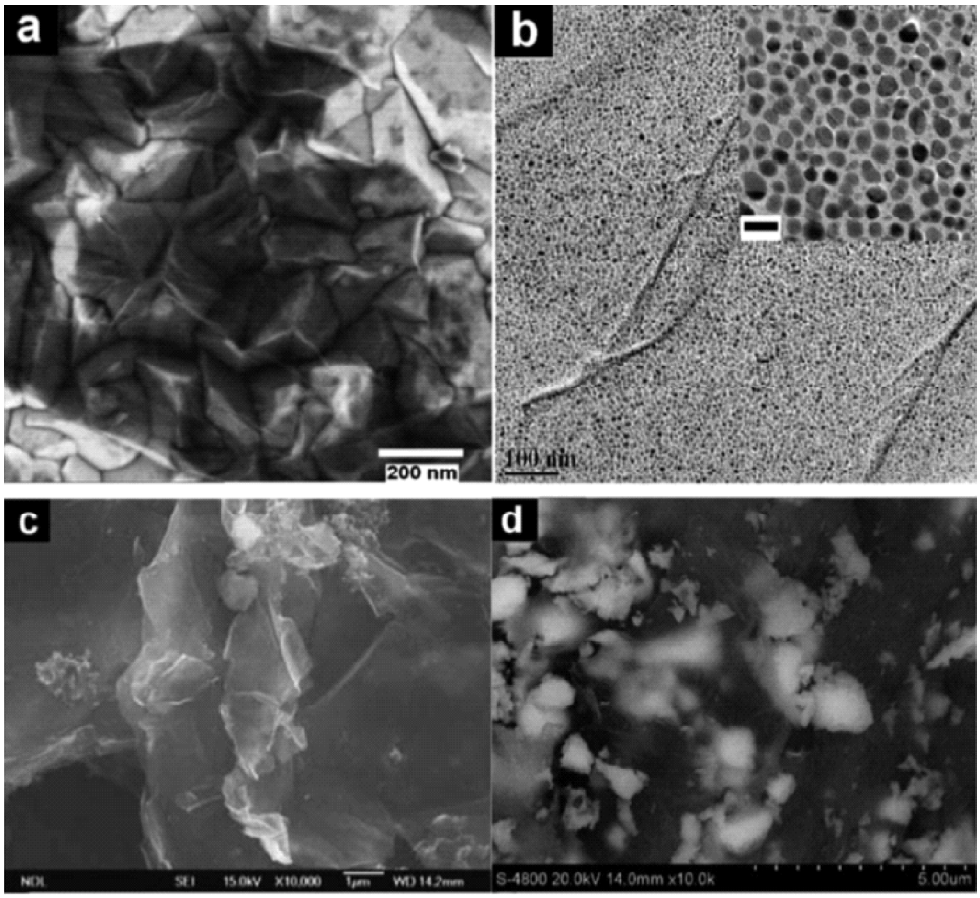


**Figure 8:** SEM images of (a) the FTO/graphene/Pt counter electrode, (b) the graphene/Pt composite, (c) the graphene/Pt composite and (d) the graphene/ $Ni_{12}P_5$ composite

electrode not only contained a lower amount of Pt, but it also exhibited an improved conversion efficiency. The efficiency improvement was attributed to the increase in the graphene sheet defects caused by Pt as the D/G ratio of the Raman spectra (Fig. 9) was increased by incorporating Pt into the graphene sheets.

Ni was also combined with graphene to form composite counter electrodes. Dou et al. employed a hydrothermal reaction for the synthesis of $Ni_{12}P_5$/graphene composites, in which $Ni_{12}P_5$ nanoparticles were embedded into the graphene sheets (Fig. 8d). Furthermore, they demonstrated that the $Ni_{12}P_5$/graphene exhibited excellent electrocatalytic activity for $I_3^-$ reduction, resulting in a high efficiency (5.7%) for the DSSC with the $Ni_{12}P_5$/graphene counter electrode (Table 3).

**Table 3**
**PV characteristics of DSSCs fabricated with graphene/metal composite counter electrodes**

| *Counter electrode* | *Jsc(mA cm$^{-2}$)* | *Voc(V)* | *FF* | *h(%)* |
|---|---|---|---|---|
| Graphene/Pt | 15.20 | 0.71 | 0.71 | 7.66 |
| Pt | 15.33 | 0.71 | 0.75 | 8.16 |
| Graphene-$Ni_{12}P_5$ | 6.67 | 0.74 | 0.59 | 2.90 |
| Graphene/Pt | 5.05 | 0.68 | 0.58 | 2.00 |
| Graphene | 12.06 | 0.79 | 0.67 | 6.35 |

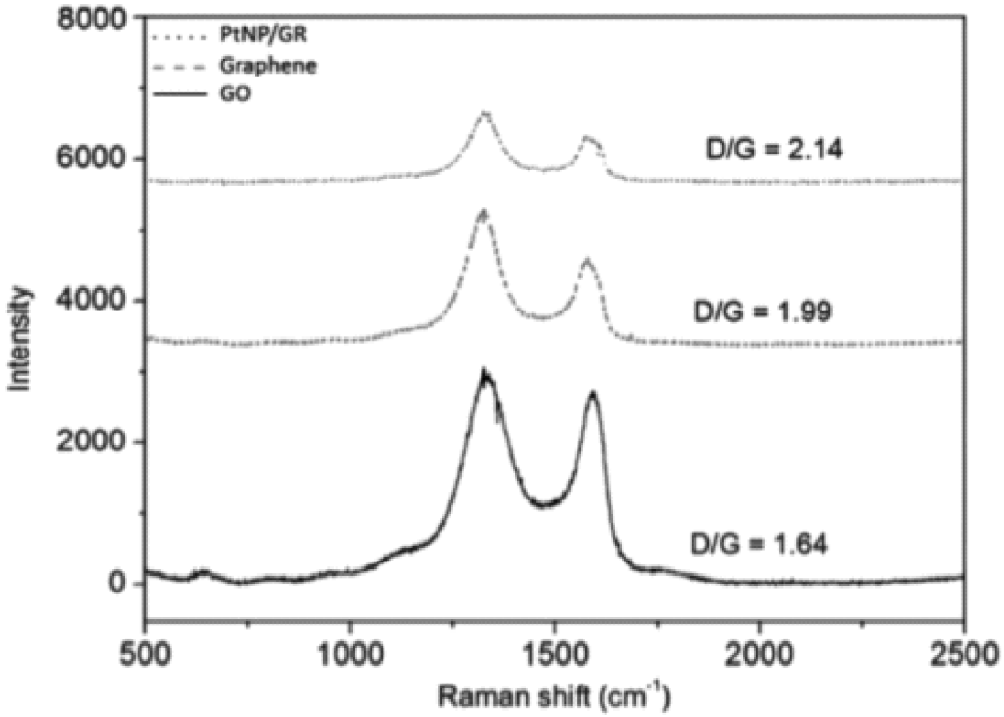


**Figure 9:** Raman spectra of GO, graphene and PtNP/GR with the corresponding D/G ratios

The role of graphene in these metal/graphene composite materials was recognized as a scaffold to well disperse metal (Pt or $Ni_{12}P_5$) particles, increasing the availability of the metal particles for electron transfer. Furthermore, graphene could also provide a fast diffusion pathway for the electrolyte and ensure excellent electrode–electrolyte contact, which improves the electron transfer rate at the interface. The metal (Pt or $Ni_{12}P_5$) nanoparticle can serve as both the active site for electrocatalytic processes and the spacer between the graphene sheets to accelerate the diffusion of the electrolyte (Fig. 10).

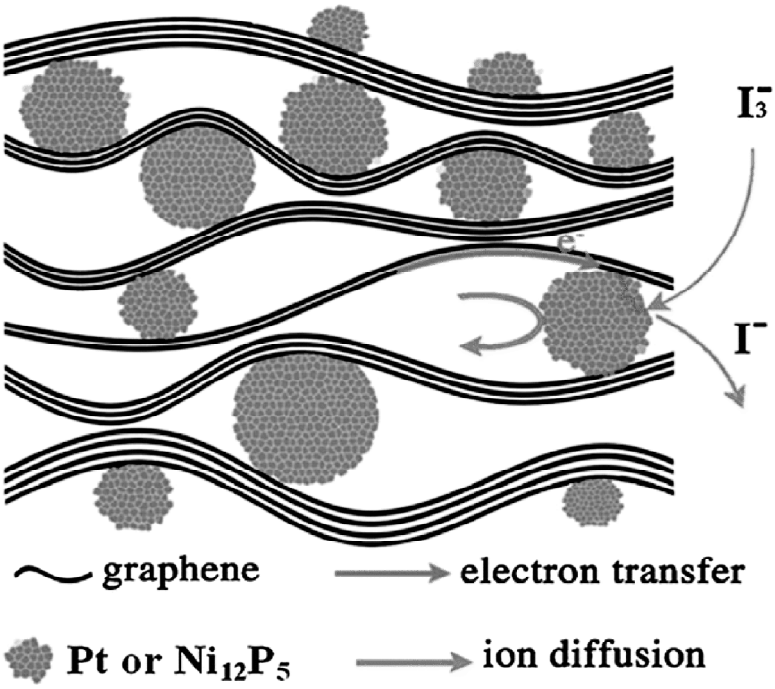


**Figure 10:** An illustration of the electrochemical reaction process in graphene/metal composites

### *5.3. Graphene/carbon nanotube composites*

Single-walled carbon nanotubes (SWCNT) and multi-walled carbon nanotubes (MWCNT) have been well investigated as catalytic materials for DSCCs. This interest has been due to SWCNT and MWCNT showed promising electrical conductivity and extremely large and tunable surface areas. Furthermore, their controllable defect edges could facilitate the electron kinetics associated with $I_3^-$ reduction. In addition, as we discussed above, graphene has been demonstrated to be a promising candidate for counter electrodes. This has stimulated recent interest in exploring graphene/CNT composites as counter electrode materials for DSSCs (Table 4).

Choi *et al.* fabricated a counter electrode using the graphene/ MWCNT composite material, in which carbon nanotubes were grown on chemical reduced graphene layers via chemical vapor deposition (CVD) (Fig. 11a). The I–V characteristics of the DSSC with

**Table 4**
**PV characteristics of DSSCs fabricated with graphene/CNT composite counter electrodes**

| *Counter electrode* | *Jsc(mA cm$^{-2}$)* | *Voc(V)* | *FF* | *h(%)* |
|---|---|---|---|---|
| Graphene/MWNTs | 5.60 | 0.76 | 0.70 | 3.00 |
| RG-CNTs | 8.95 | 0.72 | 0.70 | 4.46 |
| Pt | 12.86 | 0.78 | 0.61 | 6.17 |
| GNS40 | 15.40 | 0.77 | 0.68 | 7.88 |
| Graphene/MWNTs | 8.80 | 0.77 | 0.67 | 4.00 |

the graphene/MWCNT counter electrode are shown in Fig. 11b. The cell exhibited an energy conversion efficiency of 3.0%, which is higher than that of the DSSC with a MWCNT- based counter electrode. The efficiency improvement was attributed to the expansion of the reaction area (at the interface) due to the vertically grown MWCNTs on the graphene sheets. The performance of graphene/MWCNT counter electrodes was further improved by modifying its preparation approach, namely, graphene was first prepared on a $SiO_2$/Si substrate via CVD, followed by the growth of carbon nanotubes on top of the graphene layer.76 The DSSC with the CVD graphene/MWCNT counter electrode showed an efficiency of 4.46%. Furthermore, Zhu et al. exploited the electrophoretic deposition (EPD) method to synthesize reduced graphene–CNT composite materials as DSSC counter electrodes. **[42]** From Fig. 12, one can see that the composite material possesses a graphene–CNT network structure that can ensure an excellent contact between the graphene sheets and the CNTs. The I–V characteristics of the DSSCs with the graphene/ CNT composite counter electrodes show that, with an increasing of CNTs to graphene in the composite film, the efficiency of the DSSC increases first (reaching a maximum value of 6.17% at 60% CNTs) and then decreases (Fig. 12). The optimized content (60%) of CNTs in the graphene/CNT composite counter electrode was further confirmed by Battumur et al., who prepared graphene/CNT composite films with a doctor blade method **[43]**. The initial increase in the efficiency of the DSSC was attributed to the formation of a graphene–CNTs network structure, whereas the final decrease may be due to a lower specific surface area of CNTs in comparison to graphene sheets. Velten *et al.* also investigated graphene and MWCNT composite materials for DSSC counter electrodes **[44]**. They found that the power conversion efficiency of the DSSC with a graphene/MWCNTs composite counter electrode was 7.55%, which is higher than that using MWCNTs alone (6.62%). This was attributed to the increase of the electrical conductivity between the MWCNT bundles and the graphene sheets.

## 6. Quaternary and pentanary semiconductors

The quarternary and pentanary semiconductors like $Cu_2ZnSnS_4$ (CZTS), and $Cu_2ZnSnSSe_4$ (CZTSSe) are applicable to fabrication of low-cost CE electrode. These materials have attracted considerable interest due to its biocompatibility and eco-friendliness. In CZTS, the crystal structure kesterite and stannite have a similar unit cell but different the occupation of Zn, Cu and Sn cations. The researchers are interested to find out the effect of concentration of Cu, Zn and Sn cations, and S anions on the performance of devices

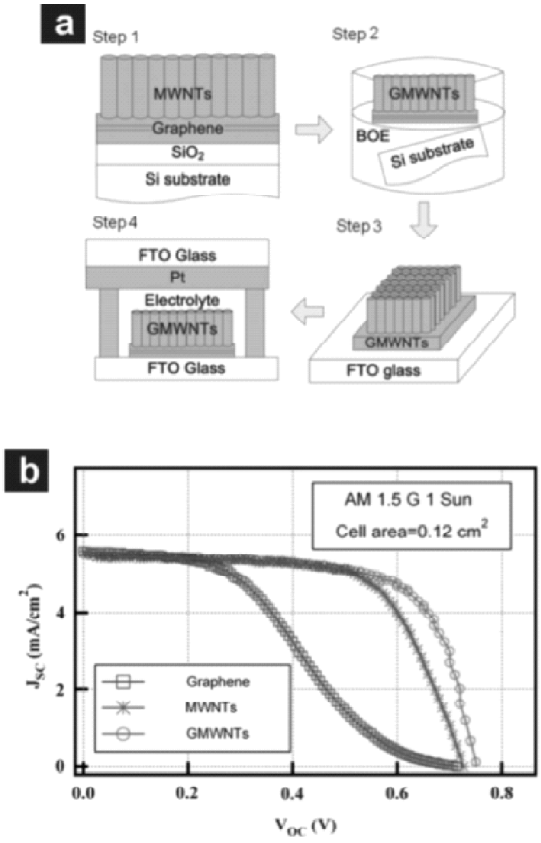


**Figure 11:** (a) A schematic diagram of the device fabrication ((1) synthesis of G–MWCNTs on $SiO_2$/Si, (2) the lift-off process of G–MWCNTs, (3) the transplant to FTO glass, (4) half the cell without $TiO_2$ and dye) and (b) the J–V characteristics of DSSCs with different counter electrodes: graphene, MWCNTs and G–MWCNTs

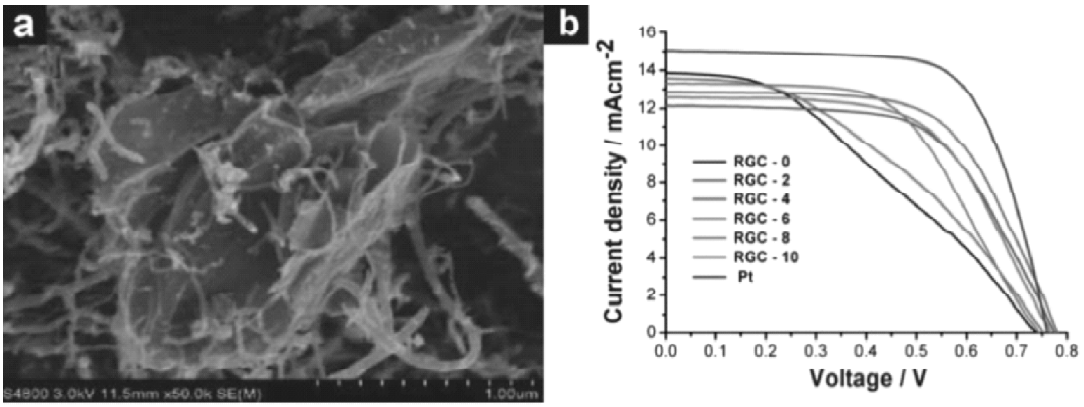


**Figure 12:** (a) An FE-SEM image of RGC-6 and (b) J–V curves of DSSCs with various graphene/CNTs counter electrodes (where the CNT contents are 0, 20, 40, 60, 80 and 100% for RGC-0, RGC-2, RGC-4, RGC-6, RGC-8 and RGC-10, respectively)

due to its tuning nature of properties like conductivity and catalytic with respect to concentrations of cations and anions respectively. Mali et al. reported the synthesis of kesterite CZTS nanofibers via electrospinning technique using polyvinylpyrrolidone (PVP) and cellulose acetate (CA) polymer at different concentrations of PVP and CA (Fig. 13a) **[45]**. The phase confirmation of CZTS has been done by XRD studies (Fig. 13b). Fig. 13c,d shows the TEM images of CZTS which were synthesized at different concentration of PVP and found that the nanofibersarefound size in between 100-150 nm diameter. The SEM image revealed that nanofibers are quite long that is in micrometer range (Fig. 13e). The DSSC devices fabricated by use of PVP-CZTS (Fig. 13f ) and CA-CZTS showed PCE of 3.10% and 3.90% respectively (Fig. 13g).The synthesis of Cu3InSnSe5 nanoparticles and their modification with Pt and Au have been reported. The IV curves revealed that pt-$Cu_3InSnSe_4$ and Au-$Cu_3InSnSe_5$ have shown comparative efficiencies of 5.8%, 7.6% that of Pt-based CE respectively.

## 7. Perovskite material

Perovskite having the $ABO_3$ type crystal structure, e.g $SrRuO_3$ where A-alkaline earth or a lanthanide; B-transition metal elements are widely used as catalysts for hydrogen evolution reactions and electro-oxidation in fuel cells to replace costly Pt catalyst**[46]**. Recently, in 2016 Guo and coworker have been reported for the first time a sputtered $SrRuO_3$ film as a counter electrode which acts as an electrocatalyst towards $I_3^-$ reduction in DSSC with efficiency 6.48%. **[47]** In this device, electrocatalysts activity depends on the lattice mismatch between the sputtered $SrRuO_3$ (SRO) film and the substrate of $MgAl_2O_4$ (MAO) single crystal through epitaxial strain. The same group reported increment of efficiency of SRO based counter electrode by insertion of graphene quantum dots (GQDs) in perovskite matrix with an efficiency of 8.05% which is higher than conventional Pt CE (7.44%). Here, $SrRuO_3$ nanoparticles have been synthesized by a facile hydrothermal technique. The SEM image revealed the formation of nanoparticles with an approximate size of 40 nm (Fig. 14A). The XRD study confirmed the formation of the orthorhombic crystal structure of $SrRuO_3$ (Fig. 14B). In order to the synthesis of SRO-GQDs nanocomposite, the water-soluble GQDs have been synthesized by the hydrothermal route. The photographic images showed the dispersed GQDs and freeze-dried GQDs results into yellow color aggregates respectively shown in Fig. 14 C, D. The TEM and HR-TEM images of GQDs shows the formation of isolated GQDs having a size in the range of 2-5 nm (Fig. 14E) and a lattice spacing distance of 0.34 nm which correspond to the graphite (002) facet (Fig. 14F). The Raman study revealed the formation of highly crystalline and graphitic structure of GQDs, since the ratio of intensities of the disordered band (D band at1375 $cm^{-1}$) and crystalline band (G band at 1572 $cm^{-1}$), (ID/IG) is equal to 0.74 (Fig. 14G). The TEM image of SRO-GQDs nanocomposite revealed that GQDs are decorated on the surface of SRO nanoparticles (Fig. 14H).The schematic representation of the electrolyte regeneration process for SRO and SRO– GQD hybrid CE is shown in Fig. 14I. The I-V characteristic of the DSSCs using different CEs measured under AM 1.5 simulated solar illumination (100 mW $cm^{-2}$). (a) SRO–GQD CE, (b) $SrRuO_3$ CE and (c) Pt CE is shown in Fig. 14J.

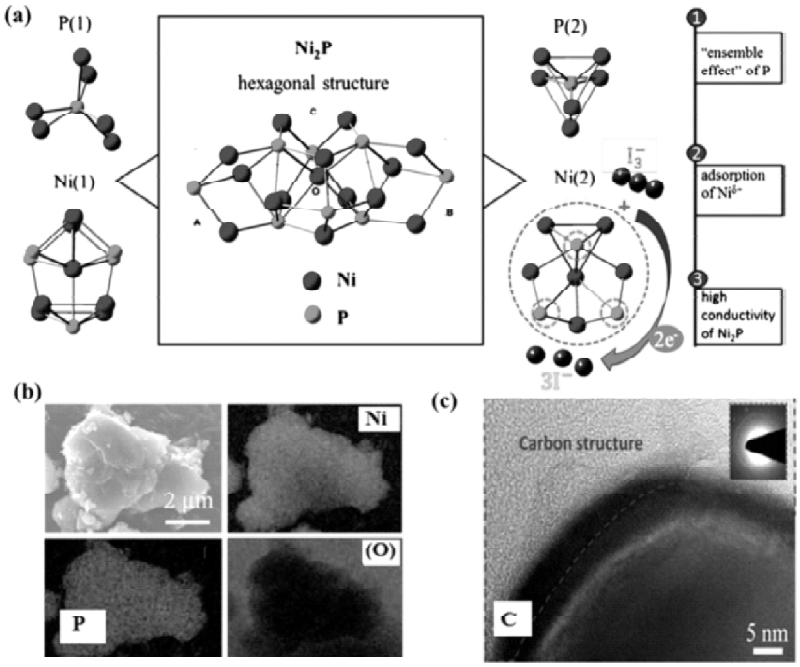


**Figure 13:** (a) Schematic illustration of experimental set-up for electrospun CZTS nanofibers as a counter electrode for DSSCs (b) XRD pattern (c,d) HRTEM analysis of CZTS nanofibers prepared from different precursors. (e) surface morphology of CZTS nanofibers (f) device architecture and (g) J-V curves for respective counter electrodes. Reprinted with permission from ref. Copyright 2014 American Chemical Society

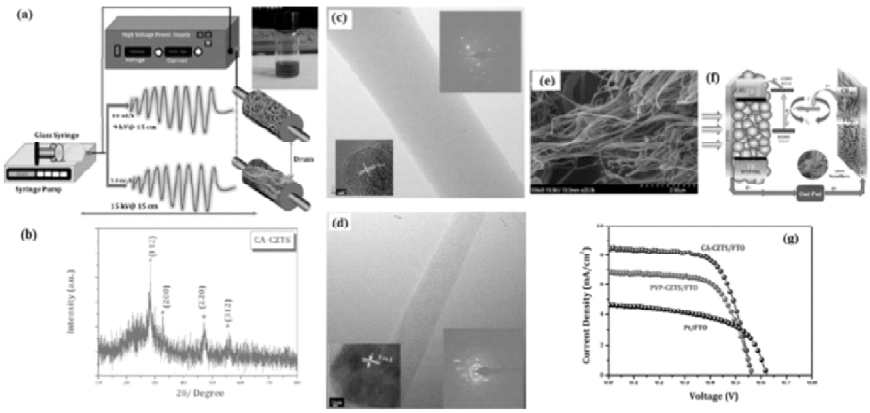


**Figure 14:** (A) Top view FESEM image of a $SrRuO_3$(SRO) CE and (B) powder XRD pattern of the as-synthesized SRO nanoparticles. Photograph of the (C)as-prepared GQD aqueous solution and (D) freeze-dried GQDs. (E) TEM image, (F) HRTEM image and (G) Raman spectrum of the synthesized GQDs. (H) TEM image of GQD decorated SRO nanoparticles (I) the schematic representation of the electrolyte regeneration process for SRO and SRO–GQD hybrid CE (J) IV characteristics of the DSSCs using different CEs measured under AM 1.5 simulated solarillumination (100 mW $cm^{-2}$). (a) SRO–GQD CE, (b) SrRuO3 CE and (c) Pt CE. Reprinted with permission from ref. Copyright 2017 Royal Chemical Society

## 8. Characterization techniques for studying the catalytic activity of CEs

### *8.1. Electrochemical impedance spectrum (EIS) technique*

EIS is the standard technique to study the intrinsically electrocatalytic activity of counter electrode, which is commonly carried out by using symmetric cells fabricated with two identical electrodes (CE/electrolyte/CE). The obtained Nyquist plot for symmetric cells in Fig. 15 an illustrates the impedance characteristics of CE, and the corresponding equivalent circuit in Fig. 15b that fitting the EIS spectra shows the detailed impedance parameters **[48]**. In a typical Nyquist plot, the impedance at high-frequency section where the phase is zero represents the series resistance ($R_h$), the left semicircle at high-frequency region corresponds to the charge transfer resistance ($R_{ct}$) in the electrode/electrolyte interface and the corresponding double layer capacitance (Cd), and the right semicircle at low-frequency zone may be attributed to the Nernst diffusion impedance ($Z_w$) of the redox couple in the electrolyte **[49]**. The $R_{ct}$ is the crucial parameter to directly evaluate electrocatalytic activity of counter electrode, and the smaller $R_{ct}$ indicates a higher catalytic ability for the triiodide reduction. Other parameters, such as Cd and $Z_w$, are related to surface area of the electrode material and diffusion velocity of the redox couple in the electrolyte, respectively. The higher surface area and faster diffusion rate contribute to the larger Cd and smaller $Z_w$, respectively, which are also advantageous for the higher catalytic activity of CE **[50]**.

### *8.2. Tafel polarization curve technique*

Tafel polarization curve is another powerful tool to investigate the electrocatalytic activity of counter electrode, which could be recorded on the similar devices to the ones used in EIS measurements. Generally, Tafel curve can be divided into three zones **[51]**. The curve at low potential (|U| < 120 mV) is the polarization zone, the curve at middle potential (with a sharp slope) is the Tafel zone, and the curve at high potential (horizontal part) is the diffusion zone. The two important parameters of exchange current density ($J_0$) and limiting diffusion current density ($J_{lim}$), which are obtained from the latter two zones, are closely related to the catalytic activity of the CE catalysts.

In the Tafel zone, a bigger slope offers a larger $J_0$, reflecting a higher catalytic activity toward the triiodide reduction (Fig. 16) **[52]**. Besides, the $J_0$ can also be extracted from Eq. (1),

$$Jo=(RT)/nFR_{ct} \quad (1)$$

where R is the gas constant, T is the absolute temperature, $R_{ct}$ is the charge-transfer resistance extracted from the EIS spectra, and F is the Faraday's constant.

In the diffusion zone, limiting current density ($J_{lim}$) depends on the diffusion coefficient of $I^-$ / $I_3^-$ redox couple in the DSSC system according to the Eq. (2)

$$D=((1/2nFc))\, J_{lim}$$

where D is the diffusion coefficient of the triiodide, l is the spacer thickness, n is the number of electrons involved in the reduction of triiodide at the electrode, F is the Faraday

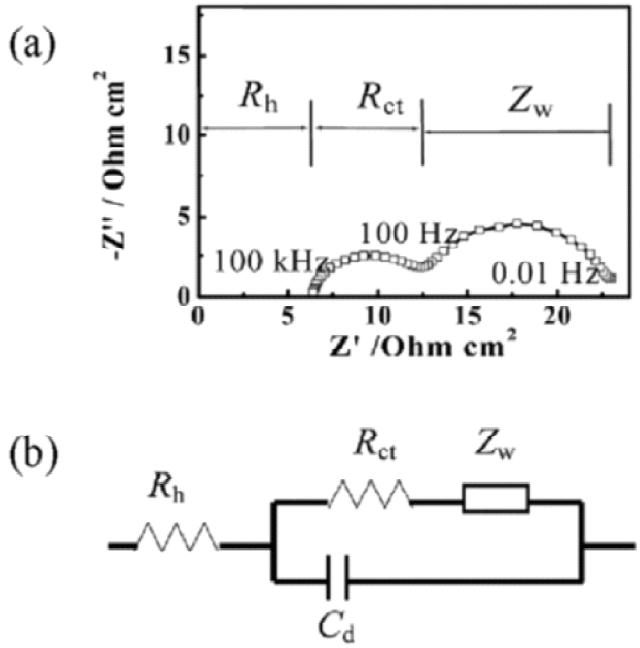


**Figure 15:** Typical Nyquist plot (a), and equivalent circuit (b). Reprinted with permission from Ref.

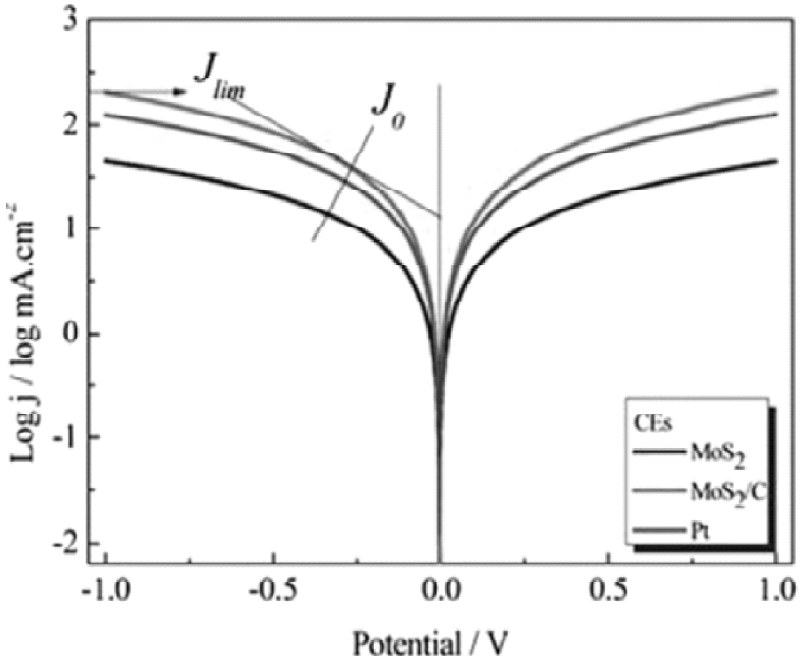


**Figure 16:** Tafel curves of the symmetrical cells based on the various electrodes. Reprinted with permission from Ref. [56]

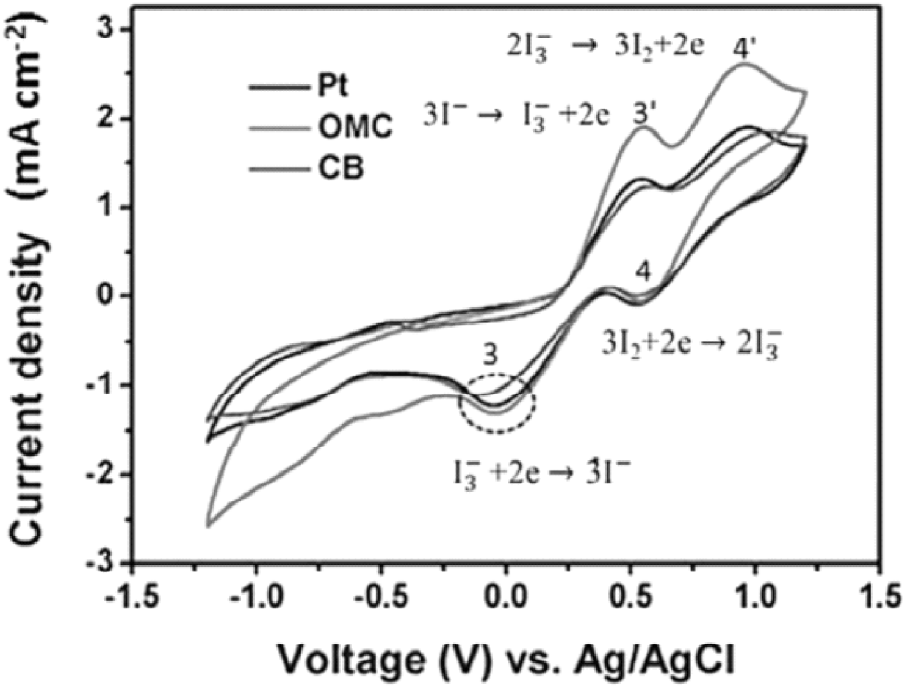


**Figure 17:** CV curves of iodide/triiodide redox species for Pt, OMC and CB counter electrodes at a scan rate of 50mVs$^{-1}$ in 10mM LiI, 1mM $I_2$ and 0.1M $LiClO_4$ in acetonitrile solution. Reprinted with permission from Ref. [61]

constant, and C is the triiodide concentration. A larger Jlim indicates a faster $I^-$ / $I_3^-$ redox couple diffusion process, which is favorable for the improvement of catalytic activity of counter electrode.

### *8.3. Cyclic voltammogram (CV) technique*

CV measurement is used to further examine the reduction reaction of $I_3^-$ on the CEs, which is usually conducted in a three- electrode system **[53]**. As shown in Fig. 17, in most cases, two pairs of oxidation and reduction peaks could be observed for CEs. The left and right pairs are ascribed to reaction 3 and 4, respectively. Especially, the reaction 3 is the rate-determining step for characterizing the electrocatalytic activity of CE, since the CE in the DSSC serves as the catalyst for catalyzing the reduction of $I_3^-$ to $I^-$ **[54]**. The peak current density and peak-to-peak separation (Epp) of the reaction 3, which is negatively correlated with the standard electrochemical rate constant of a redox reaction, are two key parameters for comparing catalytic activities of different CEs. Larger peak current density and smaller Epp demonstrate higher catalytic kinetics for the CE.

$$I_3^- + 2e^- \leftrightarrow 3I^- \quad (3)$$

$$3I_2^- + 2e^- \leftrightarrow 2I_3^- \quad (4)$$

In this review, we highlight recent progress of various carbon CEs in DSSCs and summarize the pivotal factors in determining photoelectrical performance. Furthermore, optimization of power conversion efficiency from controlling three crucial parameters ($V_{oc}$, $J_{sc}$ and FF) by regulating the physical and chemical properties of carbon materials is also discussed in detail. The review aims at conducting the rational design of carbonaceous materials (particularly porous carbon and graphene) and developing low-cost and high-catalytic carbon CEs for the triiodide reduction.

### *Outlook*

Graphene is a novel counter electrode material for the development of DSSCs with a high performance and a low cost due to its tunable structure and excellent conductivity, as well as its high film-flexibility. It was found that the defects and functional groups of the graphene sheets play a critical role in the electrocatalytic sites in DSSC counter electrodes. Therefore, tuning the defects and searching for effective functional groups for graphene sheets may be promising research directions for graphene-based DSSCs. Transition metal sulfides34–36 and nitrides are effective materials for DSSC counter electrodes. It would be reasonable to expect the further improvement of DSSC efficiency via the combination of graphene sheets with these compounds to produce effective composite counter electrodes. So far, there is very limited information regarding the electrocatalytic mechanism of graphene sheets in DSSC counter electrodes. Therefore, a deeper understanding of the role of graphene in the counter electrodes needs intensive future research.

### *Reference*

[1] F. Gong, Z. Li, H. Wang, Z. S. Wang, J. Mater. Chem. 2012, 22, 17321 – 17327.

[2] R. Bajpai, S. Roy, N. Koratkar, D. S. Misra, Carbon 2013, 56, 56 – 63.

[3] Y. Areerob, W.C Oh, JMMP 2018,8(2), 123-150.

[4] V. D. Dao, L. L. Larina, K. D. Jung, J. K. Lee, H. S. Choi, Nanoscale 2014, 6, 477 – 482.

[5] Q. Zhang, Y. Liu, Y. Duan, N. Fu, Q. Liu, Y. Fang, Q. Sun, Y. Lin, RSC Adv. 2014, 4, 15091–15097.

[6] Q. Chang, Z. Ma, J. Wang, Y. Yan, W. Shi, Q. Chen, Y. Huang, Q. Yu, L. Huang, Electrochim. Acta 2015, 151, 459– 466.

[7] Y. Areerob, K. Y. Cho, W.C Oh, J. Photochem. Photobiol., A 2017, 340, 157-169.

[8] C.J. Liu, S.Y. Tai, S.W. Chou, Y.C. Yu, K.D. Chang, S. Wang, F. S. S. Chien,

[9] J. Y. Lin, T. W. Lin, J. Mater. Chem. 2012, 22, 21057–21064.

[10] J. Y. Lin, C. Y. Chan, S. W. Chou, Chem. Commun. 2013, 49, 1440 – 1442.

[11] Z. Li, F. Gong, G. Zhou, Z. S. Wang, J. Phys. Chem. C 2013, 117, 6561–6566.

[12] Y. Li, Q. Feng, H. Wang, G. Zhou, Z. S. Wang, J. Mater. Chem. A 2013, 1, 6342–6349.

[13] Y. Li, H. Wang, Q. Feng, G. Zhou, Z. S. Wang, ACS Appl. Mater. Interfaces 2013, 5, 8217–8224.

[14] Y. Areerob, W.C Oh, JMMP 2017,8(1), 61-101.

[15] Y. Areerob, K. Y. Cho, W.C Oh, J. Mater. Sci. - Mater. Electron. 2018, 29,3437–3448.

[16] L. Bai, J. N. Ding, N. Y. Yuan, H. W. Hu, Y. Li, X. Fang, Mater. Lett. 2013, 112, 219–222.

[17] L. Zhou, X. Yang, B. Yang, X. Zuo, G. Li, A. Feng, H. Tang, H. Zhang, M. Wu, Y. Ma, S. Jin, Z. Sun, X. Chen, J. Power Sources 2014, 272, 639–646.

[18] X. Duan, Z. Gao, J. Chang, D. Wu, P. Ma, J. He, F. Xu, S. Gao, K. Jiang, Electrochim. Acta 2013, 114, 173–179.

[19] E. Bi, H. Chen, X. Yang, W. Peng, M. Gratzel, L. Han, Energy Environ. Sci. 2014, 7, 2637–2641.

[20] S. Q. Guo, T. Z. Jing, X. Zhang, X. B. Yang, Z. H. Yuan, F. Z. Hu, Nanoscale 2014, 6, 14433 – 14440.

[21] G. Wang, J. Zhang, S. Kuang, S. Liu, S. Zhuo, J. Power Sour- ces 2014, 269, 473 – 478.

[22] X. Zhang, T. Z. Jing, S. Q. Guo, G. D. Gao, L. Liu, RSC Adv. 2014, 4, 50312 – 50317.

[23] G. Li, X. Chen, G. Gao, Nanoscale 2014, 6, 3283 – 3288.

[24] C. Y. Liu, K. C. Huang, P. H. Chung, C. C. Wang, C. Y. Chen, R. Vittal, C. G. Wu, W. Y. Chiu, K. C. Ho, J. Power Sources 2012, 217, 152 – 157.

[25] H. Niu, S. Zhang, Q. Ma, S. Qin, L. Wan, J. Xu, S. Miao,RSC Adv. 2013, 3, 17228 – 17235.

[26] Y. S. Wang, S. M. Li, S. T. Hsiao, W. H. Liao, S. Y. Yang, H. W. Tien, C. C. M. Ma, C. C. Hu, J. Power Sources 2014, 260, 326 – 337.

[27] L. Wan, B. Wang, S. Wang, X. Wang, Z. Guo, H. Xiong, B. Dong, L. Zhao, H. Lu, Z. Xu, X. Zhang, T. Li, W. Zhou, React. Funct. Polym. 2014, 79, 47 – 53.

[28] S. P. Lim, A. Pandikumar, Y. S. Lim, N. M. Huang, H. N. Lim, Sci. Rep. 2014, 4, Article Number 5305.

[29] W. Liu, Y. Fang, P. Xu, Y. Lin, X. Yin, G. Tang, M. He, ACS

[30] Appl. Mater. Interfaces 2014, 6, 16249 – 16256.

[31] F. Gong, X. Xu, G. Zhou, Z. S. Wang, Phys. Chem. Chem. Phys. 2013, 15, 546 – 552.

[32] X. Xu, D. Huang, K. Cao, M. Wang, S. M. Zakeeruddin, M. Gratzel, Sci. Rep. 2013, 3, Article Number 1489.

[33] M. Wang, Q. Tang, P. Xu, B. He, L. Lin, H. Chen, Electro-chim. Acta 2014, 137, 175 – 182.

[34] C. Xu, J. Li, X. Wang, J. Wang, L. Wan, Y. Li, M. Zhang, X. Shang, Y. Yang, Mater. Chem. Phys. 2012, 132, 858 – 864.

[35] M.-Y. Yen, C.-K. Hsieh, C.-C. Teng, M.-C. Hsiao, P.-I. Liu, C.-C. M. Ma, M.-C. Tsai, C.-H. Tsai, Y.-R. Lin, T.-Y. Chou, RSC Adv. 2012, 2, 2725 – 2728.

[36] Y. Xue, J. Liu, H. Chen, R. Wang, D. Li, J. Qu, L. Dai, Angew. Chem. Int. Ed. 2012, 51, 12124 – 12127.

[37] G. Wang, W. Xing, S. Zhuo, Electrochim. Acta 2013, 92, 269 – 275.

[38] X. Zhang, S. Pang, X. Chen, K. Zhang, Z. Liu, X. Zhou, G. Cui, RSC Adv. 2013, 3, 9005 – 9010.

[39] M.J. Ju, J.C. Kim, H.J. Choi, I.T. Choi, S.G. Kim, K. Lim, J. Ko, J. J. Lee, I. Y. Jeon, J. B. Baek, H. K. Kim, ACS Nano 2013, 7, 5243 – 5250.

[40] L. Song, Q. Luo, F. Zhao, Y. Li, H. Lin, L. Qu, Z. Zhang, Phys. Chem. Chem. Phys. 2014, 16, 21820 – 21826.

[41] J. Ma, C. Li, F. Yu, J. Chen, J. Power Sources 2015, 273, 1048 – 1055.

[42] Q. Luo, F. Hao, S. Wang, H. Shen, L. Zhao, J. Li, M. Grat- zel, H. Lin, J. Phys. Chem. C 2014, 118, 17010 – 17018.

[43] H. Fang, C. Yu, T. Ma, J. Qiu, Chem. Commun. 2014, 50, 3328 – 3330.

[44] S.M. Jung, I.T. Choi, K. Lim, J. Ko, J.C. Kim, J.J. Lee, M. J. Ju, H. K. Kim, J. B. Baek, Chem. Mater. 2014, 26, 3586 – 3591.

[45] M.J.Ju, I.Y.Jeon, J.C.Kim, K.Lim, H.J.Choi, S.M.Jung, I.T. Choi, Y.K. Eom, Y.J. Kwon, J. Ko, J.J. Lee, H.K. Kim, J. B. Baek, Adv. Mater. 2014, 26, 3055 – 3062.

[46] M.J. Ju, I.Y. Jeon, K. Lim, J.C. Kim, H.J. Choi, I.T. Choi, Y.K. Eom, Y.J. Kwon, J. Ko, J.J. Lee, J.B. Baek, H.K. Kim, Energy Environ. Sci. 2014, 7, 1044 – 1052.

[47] Z. Wang, P. Li, Y. Chen, J. He, J. Liu, W. Zhang, Y. Li, J.Power Sources 2014, 263, 246– 251.

[48] Y. Areerob, K. Y. Cho, W.C Oh, NJC. 2017,41, 9613-9622.

[49] H.W. Liu, S.P. Liang, T.J. Wu, H. Chang, P.K. Kao, C.C. Hsu, J. Z. Chen, P. T. Chou, I. C. Cheng, ACS Appl. Mater. Interfaces 2014, 6, 15105–15112.

[50] M. H. Yeh, L. Y. Lin, L. Y. Chang, Y. A. Leu, W. Y. Cheng, J. J. Lin, K. C. Ho, ChemPhysChem 2014, 15, 1175 – 1181.

[51] F. Gong, H. Wang, Z. S. Wang, Phys. Chem. Chem. Phys. 2011, 13, 17676–17682.

[52] G.H. Guai, Q.L. Song, C.X. Guo, Z.S. Lu, T. Chen, C.M. Ng, C. M. Li, Sol. Energy 2012, 86, 2041 – 2048.

[53] V. Tjoa, J. Chua, S. S. Pramana, J. Wei, S. G. Mhaisalkar, N. Mathews, ACS Appl. Mater. Interfaces 2012, 4, 3447–3452.

[54] V. D. Dao, N. T. Q. Hoa, L. L. Larina, J. K. Lee, H. S. Choi, Nanoscale 2013, 5, 12237–12244.